Engineering Failure Analysis 180 (2025) 109825

Contents lists available at ScienceDirect

Engineering Failure Analysis

journal homepage: www.elsevier.com/locate/engfailanal

High- and low-cycle fatigue behavior of additively manufactured Ti6Al4V and influence of surface finish

L. Pagliari [a,*], R. Gerosa [b], D. Panzeri [b], L. Fraccaroli [a], F. Concli [a]

[a] Faculty of Engineering, Free University of Bolzano/Bozen, 39100 Bolzano, Italy
[b] Dipartimento di Meccanica, Politecnico di Milano, Polo Territoriale di Lecco 23900 Lecco, Italy

ARTICLE INFO

Keywords:
Titanium Alloy
Fatigue failure
Fracture mechanics
Roughness
SEM

ABSTRACT

Ti6Al4V has emerged as one of the most promising materials for Additive Manufacturing (AM). In this work, three series of AM Ti6Al4V samples were employed to assess the material fatigue behavior and its dependency on surface finish. One series was left in as-built conditions, one was machined, and one was finely polished. No samples underwent heat treatment, and their dimensions were chosen to be representative of the characteristic strut size of AM reticular structures. The as-built and machined series were characterized in terms of roughness, monotonic, Low-Cycle Fatigue (LCF) and High-Cycle Fatigue (HCF) behaviors. The polished series was intended to determine the fatigue limit under ideal surface finish conditions, undergoing roughness and HCF tests only. This allowed the determination of the fatigue limit reduction factors due to surface finish, providing designers with a practical tool for evaluating the effect of surface roughness on the fatigue performance of AM Ti6Al4V. Besides, scanning electron microscopy and fracture mechanics analysis through Kitagawa-Takahashi diagrams, based on Murakami's theory, were performed. Different laws correlating defect size and fatigue limit of defective components were compared. By transforming roughness into an equivalent defect, further insight into the effect of surface finish on fatigue performance was gained.

1. Introduction

In recent years, Additive Manufacturing (AM) has gained an important role in the production of mechanical components. Indeed, this technology has very few constraints in terms of geometries that can be manufactured, enabling the manufacturing of products with very complex shapes [1]. In addition, AM enables the production of such complex geometries without the waste of material that is typical of traditional manufacturing techniques. These capabilities make AM not only interesting from a technical point of view, but also cost-effective in a large variety of circumstances [2]. Components are built layer upon layer, enabling new possibilities in terms of optimization and weight reduction through the employment of lattice and reticular structures [3,4]. These distinctive advantages have promoted interest in AM technologies. Increasing research efforts focus on assessing their applicability in sectors where non-AM materials have traditionally been employed [5,6] and in developing an increasing number of AM materials, ranging from metals to ceramics, including polymers and Multi-Materials [7–10]. Steels, aluminum alloys and titanium alloys are among the materials that are most studied for AM production through fusion of powders [11–13]. However, while the chemical composition of most of the alloys on

* Corresponding author.
E-mail addresses: l.pagliari@unibz.it (L. Pagliari), riccardo.gerosa@polimi.it (R. Gerosa), davide.panzeri@polimi.it (D. Panzeri), lorenzo.fraccaroli@unibz.it (L. Fraccaroli), franco.concli@unibz.it (F. Concli).

https://doi.org/10.1016/j.engfailanal.2025.109825
Received 3 May 2025; Received in revised form 11 June 2025; Accepted 18 June 2025
Available online 19 June 2025
1350-6307/

the market is similar to that of wrought materials, the different solidification process typical of AM leads to different mechanical properties [14,15]. For this reason, a comprehensive characterization of their mechanical behavior is essential for an effective utilization as a viable alternative to conventional manufacturing methods. Among others, the quasi-static (QS), the Low-Cycle-Fatigue (LCF) and the High-Cycle-Fatigue (HCF) behaviors are the fundamental parameters that should be known for a reliable design of new components.

Ti6Al4V is among the titanium alloys that are most employed in industry. Ti6Al4V is an $\alpha + \beta$ phase alloy characterized by a high strength, relatively low density, good fracture toughness, and excellent corrosion resistance [16]. It is widely employed in aeronautical applications, thanks to its lightweight characteristics [17–19]. More recently, with new advancements in the field of orthopedic implants, this alloy is becoming the standard choice for artificial prostheses thanks to its excellent bio-compatibility [20–24]. The traditional manufacturing process of Ti6Al4V involves forging, casting, and rolling of bulk feedstock materials before undergoing machining operations [25]. However, in recent years it has become one of the most widespread alloys in AM, thanks to its printability which makes it compatible with AM techniques, ranging from Direct-Energy-Deposition (DED) to Selective-Laser-Melting (SLM), including Electron-Beam-Melting (EBM) [26–28]. These processes are characterized by using a laser or electron beam source to melt the material, reaching very high melting and solidification speeds [29–31]. Such manufacturing parameters strongly influence the microstructure of printed products, leading to residual stresses, which affect the macroscopic response of the structure [32,33]. In addition, another typical and dangerous aspect of AM parts is the presence of defects such as internal pores and high surface roughness, which have a pejorative impact on the mechanical and fatigue properties [34,35]. This is especially true for the surface defects (such as surface roughness) that are in most case the sites of nucleation of cracks, representing a detrimental feature for fatigue resistance [36,37].

The effect surface finish on fatigue properties is investigated in the present work. Three series of Ti6Al4V samples manufactured via SLM and having different surface finishes were characterized in terms of QS, LCF, HCF and behaviors. Comparison of the behavior of the different series of specimens allowed to quantify the effect of the surface roughness on the mechanical performances of AM Ti6Al4V.

2. Materials and methods

To characterize the HCF and LCF behaviors as well as the influence of surface finish in AM Ti6Al4V, three series of cylindrical samples were manufactured via SLM. The first series was left in the as-built condition, and was produced with two geometries, one for HCF tests and the other for LCF tests. The geometry for HCF specimens is represented in Fig. 1a and was designed according to the ASTM E466 standard [38]. The geometry for LCF specimens is represented in Fig. 1b and was designed according to ASTM E606 standard [39]. All proportions prescribed by the standard were respected, but the recommended minimum dimensions of the specimens were reduced. This choice was made to reproduce more closely the typical operating conditions of AM materials, which are frequently used to manufacture reticular structures having struts with small diameters. Because size plays a fundamental role in the fatigue behavior of materials, to obtain a similar fatigue response small-diameter specimens were produced. This choice had already been tested in previous experiments leading to good results [40–42]. The second series of specimens was produced with the same HCF and LCF geometries and was machined to achieve better surface conditions. Eventually, the third series of specimens was produced only with HCF geometry and was finely polished, to obtain optimal surface conditions (i.e., $R_a < 0.2$ according to ASTM E606 standard). This series was intended to determine the fatigue limit of the material in ideal surface conditions, which was used to evaluate

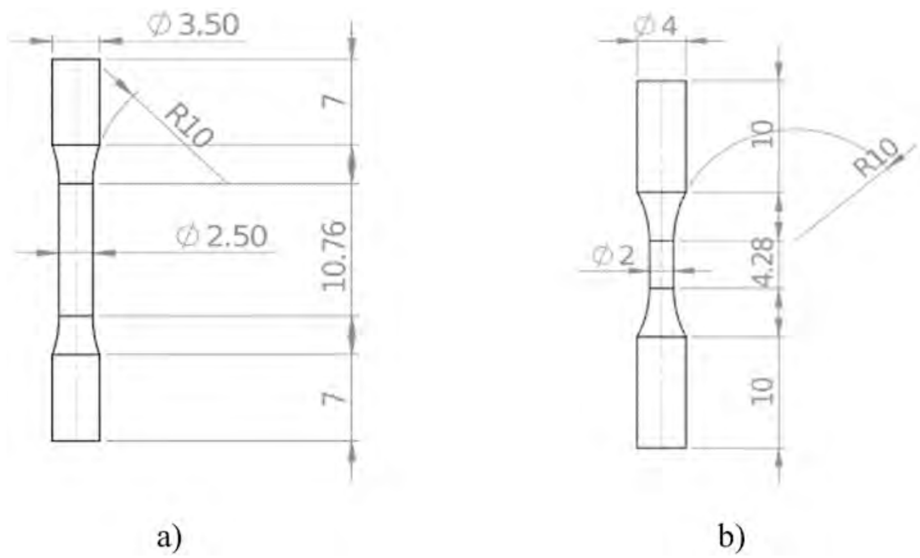

Fig. 1. Samples geometries: for HCF and QS tests (a), for LCF tests (b).

fatigue limit reduction factors due to surface finish and to perform fracture mechanics analysis.

All specimens were produced via SLM using an EOS M290 machine. The process parameters were optimized by the supplier, with the aim of minimizing the quantity of internal porosities and defects, as proved by the mirror-polished transversal sections observable in Section 3.4, showing almost no residual porosity. This aspect was fundamental in determining the ideal fatigue limit. The build direction corresponded to the longitudinal axis of each specimen, while the scanning plane lied on the transversal plane. Ti6Al4V powder particles had a spherical morphology with size from 15 μm to 45 μm, and their chemical composition is reported in Table 1. None of the specimens underwent heat treatment.

2.1. Tensile and surface roughness tests

The tensile tests were carried out on samples with geometry reported in Fig. 1a. The tests were conducted at 25 °C and the crosshead speed was set to 0.1 mm·min^{-1}. The Ramberg-Osgood parameters of the quasi-static curve were calculated in order to satisfy the Ramberg-Osgood [43] law:

$$\varepsilon_a = \varepsilon_{ae} + \varepsilon_{ap} = \frac{\sigma_a}{E} + \left(\frac{\sigma_a}{K_{RO}}\right)^{\frac{1}{n_{RO}}} \tag{1}$$

where ε_a is the total strain amplitude, ε_{ae} and ε_{ap} are the elastic and the plastic strain components, σ_a is the stress amplitude, E is the Young's modulus, K_{RO} and n_{RO} are the Ramberg-Osgood parameters, i.e., the strength coefficient and the strain hardening coefficient, respectively. Additionally, because surface conditions are one of the most important factors affecting the fatigue resistance of materials, multiple surface roughness measurements were carried out, in order to assess the difference in the surface finish conditions between as-built and machined specimens.

2.2. HCF tests

HCF tests with a stress ratio $R = 0$ were performed on a STEPLab UD04 testing machine, capable of applying a maximum load of 5 kN at a maximum frequency of 35 Hz, used in previous studies for similar material characterizations [40–42]. The stair-case approach in combination with statistical elaboration of data according to Dixon [44] was used to determine the fatigue limit. Such method, in addition to averaging measured values, takes also into consideration the order of failures/run-outs providing a correction coefficient based on the statistical elaboration of numerous results. This short stair-case approach was previously used by the authors [45–48]. As in the traditional stair-case, the coupons were tested at different load levels. The value of the load to be applied at the $i-th$ test depends on the load of the previous one. The stress increment, $\Delta\sigma$, was assumed equal to 10 MPa. The first test is performed at the starting force level, F_1 which is determined according to literature data. If a coupon does not fail within 5×10^6 cycles (the so-called run-out condition), the subsequent test $(i+1)$ is performed at a force level increased by the force increment, i.e. $F_{i+1} = Fi + \Delta F$. Conversely, if the test does not achieve the run-out condition (i.e. ends with a failure), the subsequent test is conducted at a force decreased by the force interval, i.e. $F_{i+1} = F_i - \Delta F$. In the present work, five tests for each condition (as-built and machined) have been conducted. After the last test, the sequence order failures/run-outs is defined. The Dixon method [44] estimates the fatigue limit $(\Delta\sigma_f)$ through a coefficient, k (which can be extracted from tables and depends on the sequence order) as showed in Equation (2).

$$\Delta\sigma_f = x_F + k \bullet \Delta\sigma \tag{2}$$

where x_F is the stress level of the last test in the sequence. Moreover, Wöhler diagrams [49] were computed after performing some tests in the finite-life region.

2.3. LCF tests

LCF tests were conducted in strain control. The strain ratio was set to $R = -1$. The test frequency was set equal to the minimum value prescribed by the standard, in order to prevent overheating that could affect the results of the tests. Specifically, a frequency of 0.1 Hz [50], the minimum allowed by the standard, was selected. Both series of samples (as-built and machined) show marked hysteresis. The fitting of the corners of the stabilized cycles was performed applying the Ramberg-Osgood [44] law to cyclic loading:

$$\varepsilon_a = \varepsilon_{ae} + \varepsilon_{ap} = \frac{\sigma_a}{E} + \left(\frac{\sigma_a}{K'_{RO}}\right)^{\frac{1}{n'_{RO}}} \tag{3}$$

where K'_{RO} and n'_{RO} are the Ramberg-Osgood cyclic parameters, analogous to static constants K and n. After reaching the stabilized loop, all the tests were continued until the final failure. The number of cycles at rupture, N_f, is indeed needed for the calibration of the

Table 1
Chemical composition of the metal powder employed for AM specimens production.

Material	Ti [%]	Al [%]	Fe [%]	V [%]	C [%]
Ti6Al4v	Bal	6	<0.3	4	<0.08

Basquin-Coffin-Manson (BCM) parameters:

$$\varepsilon_a = \frac{\Delta\varepsilon_a}{2} = \frac{\sigma_f'}{E}(2N_f)^b + \varepsilon_f'(2N_f)^c \tag{4}$$

where σ_f' is the fatigue strength coefficient, b is the fatigue strength exponent, ε'_f is the fatigue ductility coefficient and c is the fatigue ductility exponent [51–53].

The calibration procedure foresees the estimation of the Basquin coefficients (σ_f' and b) first starting from the yield strength (obtained from the QS tests) and the HCF limit. The Basquin model, represented in Equation (4), is fundamental to unbundle the elastic deformation from the total one.

$$\varepsilon_{ap} = \varepsilon_a - \varepsilon_{ae} = \varepsilon_f'(2N_f)^c \tag{5}$$

The ASTM 739 standard [54], could be exploited to have the best estimation (maximum likelihood) of the coefficients of Equation (5).

$$log(N_f) = A + Blog(\varepsilon_{ap}) \tag{6}$$

$$A = \overline{X} - B\overline{Y} \tag{7}$$

$$B = \frac{\sum(x_i - \overline{X})(y_i - \overline{Y})}{\sum(x_i - \overline{X})^2} \tag{8}$$

where $\overline{X}$ and $\overline{Y}$ are the average values of the variables $x_i = log(\varepsilon_{ap})$ and $y_i = log(N)$. Equation (6) can be rearranged as:

$$\varepsilon_{ap} = 10^{\left(-\frac{\hat{A}}{B}\left(\frac{1}{2}\right)^{\frac{1}{B}}(2N_f)^{\frac{1}{B}}\right)} \tag{9}$$

In this way the maximum likelihood estimators result in:

$$\varepsilon_f' = 10^{\left(-\frac{\hat{A}}{B}\left(\frac{1}{2}\right)^{\frac{1}{B}}\right)} \tag{10}$$

2.4. Fracture mechanics analysis and Kitagawa-Takahashi diagrams

Because surface roughness and subsurface defects critically influence the fatigue behavior and performance of components, fracture mechanics analyses were carried out on the tested specimens. Assuming such defects as a single equivalent flaw, fracture mechanics principles allow a deeper understanding of the fatigue life. In particular, the approach suggested by Murakami [55] assigns to each defect a corresponding stress-intensity factor K, as showed in Equation (11):

$$K = \sigma Y\sqrt{\pi\sqrt{area}} \tag{11}$$

where σ is the applied stress and Y is a constant equal to 0.65 for surface defects and 0.5 for internal defects (meaning that surface defects have a more detrimental effect than inner ones). $\sqrt{area}$ is a parameter related to the defect shape, size and position. Specifically, it represents the effective length of the equivalent micro-notch calculated as the square root of the convex area of the defect (A_{eff}) determined according to Murakami's approach [55], as shown in Fig. 2.

As can be observed, convex areas (i.e., the surface included by the convex contour that envelopes the irregular shape of the defects)

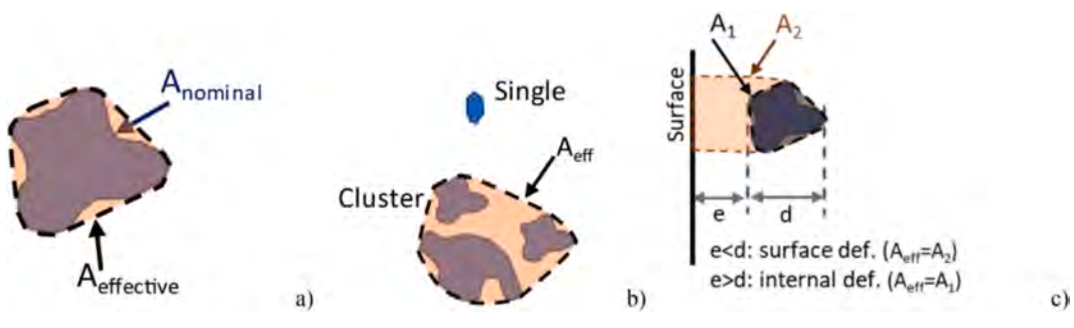

Fig. 2. Definition of the convex effective area of single defects (a) and cluster of defects (b) with and without presence of defect-surface interaction (c), according to the Murakami's method [48].

are calculated differently for single defects (Fig. 2a), clusters of defects (Fig. 2b) and considering the presence of defect-surface interaction (Fig. 2c). With regard to clusters of defects, they are obtained when distances between adjacent defects are lower than the equivalent diameter of the smallest defect within the cluster. As far as surface shallow defects (such as the surface roughness and surface defects with length-to-width ratio higher than 10) are concerned, Murakami [55] prescribes to calculate a stress intensity factor induced by such defects by using the defect depth, t, as described by Equations (12) and (13):

$$K = \sigma Y \sqrt{\pi \sqrt{area_{shallow}}} \tag{12}$$

$$\sqrt{area_{shallow}} = \sqrt{10} t \tag{13}$$

Since crack nucleation is generally driven by the worst defect, the maximum R_v parameter was selected to represent the notch effect of surface roughness [56]. The total length of each surface defect was obtained adding the length of the equivalent micro-notch to the roughness equivalent micro-notch. Areas and lengths of defects were measured by Scanning- Electron-Microscopy (SEM).

The stress-intensity factor K is very useful to study the fatigue behavior. Particularly, by using the threshold ΔK (ΔK_{th}), it is possible to define a relation between the threshold fatigue stress range ($\Delta\sigma_{th}$) and the corresponding crack length (a) through the Kitagawa-Takahashi (K-T) diagram shown in Fig. 3a [57]. El-Haddad et al. [58] suggested a relation between fatigue stress and crack length on the Kitagawa-Takahashi diagram through Equation (14):

$$\Delta\sigma_{th} = \frac{\Delta K_{th,LC}}{Y\sqrt{\pi(a + a_0)}} \tag{14}$$

where $\Delta K_{th,LC}$ is the ΔK_{th} for long cracks (Fig. 3b). a_0 is an intrinsic crack, which considers the overall effect of existing defects, microstructure, non-metallic inclusions and micro-damages induced by the manufacturing process:

$$a_0 = \frac{1}{\pi}\left(\frac{\Delta K_{th,LC}}{Y\Delta\sigma_{f0}}\right)^2 \tag{15}$$

where $\Delta\sigma_{f0}$ is the theoretical fatigue limit (i.e., the fatigue limit determined in ideal surface conditions).

However, when cracks are not associated to complete crack closure build-up (e.g., short cracks), ΔK_{th} is reduced with respect to that of long cracks ($\Delta K_{th,LC}$) [59,60], i.e., the value of the threshold ΔK depends on the crack length. To fill this gap, multiple approaches were proposed to describe the crack closure build-up [61–63], like the curve shown in Fig. 4 (called R-curve). The R-curve relates the threshold stress intensity range to the crack extension. As cracks get longer, their threshold ΔK tends to $\Delta K_{th,LC}$, while as they get shorter, they tend to $\Delta K_{th,eff}$, which is the intrinsic (effective) threshold. $\Delta K_{th,eff}$ does not depend neither on the microstructure nor the load ratio, but only on material physical properties. The scientific literature proposes different relations to determine its value. Li et al. [64] reported some models mainly based on the elastic modulus, as shown in Equation (16).

$$\Delta K_{th,eff} = \alpha\sqrt{|b|}E \tag{16}$$

where b is the Burgers vector and α is equal to 0.75 according to Pippan et al. [65]. The Burgers vector, defined by Equation (17), is a function of the lattice parameters:

$$|b| = \frac{\gamma}{2}\sqrt{h^2 + k^2 + l^2} \tag{17}$$

where γ is the edge length of the unit cell, while h, k and l are the Burgers vector components. In the HCP lattice (typical of Titanium), dislocation glide most frequently occurs on the prism planes $(10\bar{1}0)$, with Burgers vector of the type AB [66].

As a result, for short cracks, models that do not consider the dependency of the threshold ΔK on the crack length (such as El-Haddad's one) overestimate it and result non-conservative with respect to models that do consider it (such as those based on Chapetti's

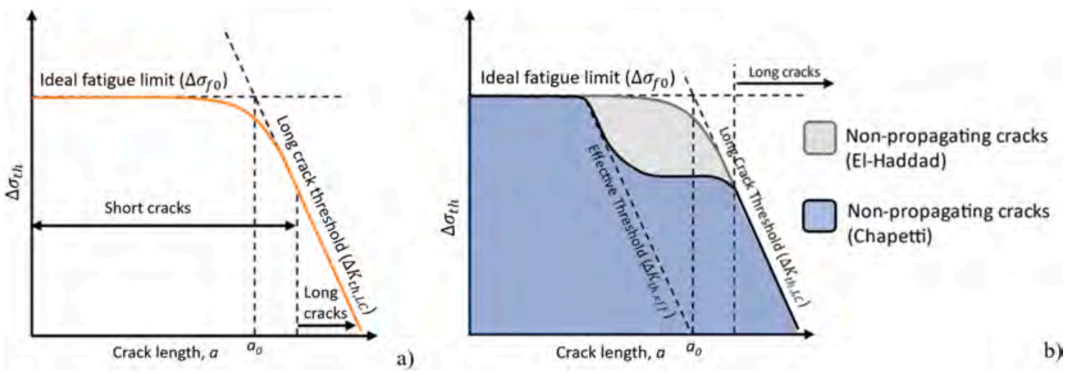

Fig. 3. Kitagawa-Takahashi diagram with El-Haddad curve (left) and Kitagawa-Takahashi diagram with El-Haddad vs Chapetti curves (right) [48].

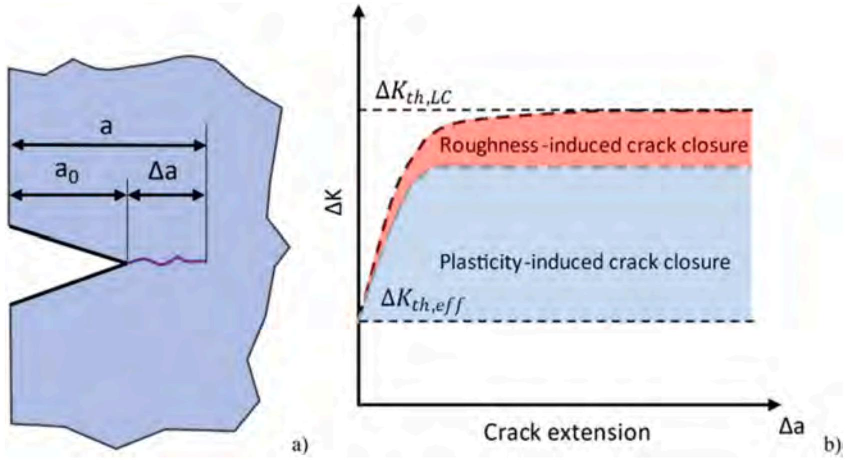

Fig. 4. Definition of the crack length, the initial crack and the crack extension (a); R curve between the stress intensity range and the crack extension (b) [48].

approach [61]), as shown in Fig. 3b. El-Haddad curve can be modified to take into account the variation of ΔK_{th} described by the R-curve [67]:

$$\Delta\sigma_{th} = \frac{\Delta K_{th}(a)}{Y\sqrt{\pi(a + a_0)}} \tag{18}$$

The limit curve based on the intrinsic (effective) $\Delta K_{th,eff}$ results in the non-propagating Chapetti region shown in Fig. 3b. Replacing the El-Haddad parameter a_0 with the modified value a_0', a new limit stress curve is obtained as shown in Equation (19) and Equation (20).

$$a'_0 = \frac{1}{\pi}\left(\frac{\Delta K_{th}(a)}{Y\Delta\sigma_{f0}}\right)^2 \tag{19}$$

$$\Delta\sigma_{th} = \frac{\Delta K_{th}(a)}{Y\sqrt{\pi(a + a'_0)}} \tag{20}$$

In this work, the R-curve for Ti-6Al-4 V was generated using the model defined by Zerbst et al. [63]:

$$\Delta K_{th} = \Delta K_{th,LC}\sqrt{\frac{\Delta a + a^*}{\Delta a + a^* + a_0}} \tag{21}$$

where Δa is the crack extension and a^* is an additional parameter adopted to make $\Delta K_{th} = \Delta K_{th,eff}$ when $\Delta a = 0$:

$$a^* = a_0\frac{\left(\Delta K_{th,eff}/\Delta K_{th,LC}\right)^2}{1 - \left(\Delta K_{th,eff}/\Delta K_{th,LC}\right)^2} \tag{22}$$

The K-T diagrams for some of the broken fatigue specimens shown in Section 4 were generated. In particular, the fractures of three different specimens were analyzed, two belonging to the as-built series (specimen ID HCF-AB and HCF-AB2) and one to the machined one (specimen ID HCF-M) as shown in Table 2. Pictures of specimen HCF-AB, HCF-AB2 and HCF-M can be found in Section 3.5. The value of $\Delta K_{th,eff}$ was calculated through Equation (15) using the lattice parameters reported in [66,68], obtaining a value of 1.28 MPa $\sqrt{m}$. For $\Delta K_{th,LC}$ the value of 3.48 MPa $\sqrt{m}$ was considered, as found by Wycisk et al. [69]. The values are reported in Table 2. With regard to the theoretical fatigue limit $\Delta\sigma_{f0}$ (which is required to for the K-T diagram), it should be determined considering fatigue specimens with the same microstructural features of the investigated materials, but without surface and inner defects. This condition was achieved through the third series of specimens, which, besides having almost no residual porosities as discussed in Section 2, were

Table 2
Kitagawa – Takahashi diagram analysis input parameters.

Specimen ID	Material	$\Delta K_{th,eff}$ [MPa $\sqrt{m}$]	$\Delta K_{th,LC}$ [MPa $\sqrt{m}$]	$\Delta\sigma_{f0}$ [MPa]
HCF-AB	as-built	1.28	3.48	Determined via polished specimens
HCF-AB2	as-built			
HCF-M	machined			

finely polished to achieve near-to-ideal surface conditions ($R_a < 0.2$).

3. Results

3.1. Tensile and surface roughness tests

The elastic modulus (E), the yield strength (σ_Y), the Ultimate Tensile Strength (UTS) and the Ramberg-Osgood obtained through tensile, quasi-static tests are shown in Table 3. The obtained values of σ_Y and UTS are aligned with those found in literature [70]. Machined samples displayed a slightly better performance, although the effect of surface conditions on static properties is very limited. Yet, the coarse surface of as-built samples could feature defects large enough to act as stress raisers significant enough to affect static properties.

The results of surface roughness measurements are reported in Table 4. The surface roughness, especially in the as-built condition, is very high as remarked also by the micrographs in Section 3.4. The roughness of polished samples is also reported, since they were fabricated to find the fatigue limit in near-to-ideal conditions, which require very fine surface finish conditions.

3.2. HCF tests

With regard to HCF tests performed using the short stair-case approach, for as-built specimens the sequence of failures and run-outs is O-X-O-O-O (Fig. 5). The Dixon's factor results equal to -0.157 leading to a fatigue limit, according to Equation (2), of 161 MPa (expressed as maximum applied stress). The value falls within the range of those that can be found in literature for SLM as-built samples tested at R = 0.1 (a load ratio that leads to fatigue results very similar to those obtained with R = 0, which was employed in this work) [71–73]. Indeed, Bagehorn et al. [71] obtained a fatigue limit of 175 MPa, Wycisk et al. [72] obtained a fatigue limit of 210 MPa, while Gong et al. [73] obtained a fatigue limit as low as 100 MPa. The high variability in literature values of fatigue limits of SLM Ti6Al4V as-built specimens is due to differences in the type of powder, printing process parameters and surface conditions. Still, the obtained fatigue limit fits well in such range.

Regarding the machined series, the test order is O-X-X-O-O (Fig. 5). The Dixon factor results equal to 0.305 leading to a fatigue limit of 319 MPa, almost double the limit for as-built specimens. The comparison with literature data is a delicate process, since available literature data referring to machined specimens, is also associated to heat treated specimens. As a result, the values that are found in literature are higher, but due to the enhancement in fatigue properties that heat treatments grant. For instance, Greitemeier et al. [74] measured a limit of 550 MPa (R = 0.1) for SLM specimens that were milled, but which also received an annealing heat treatment at 710 °C for 2 h in vacuum. Wycisk et al. [72] found a fatigue limit of 510 MPa (R = 0.1) for SLM specimens that were polished, but which also were annealed at 650 °C for 3 h in vacuum. However, it is to be noted that, in both the just mentioned works the fatigue limit for machined specimens was about twice the fatigue limit of the as-built specimens that received the same heat treatment, the same proportion that was found in this work.

Eventually, the stair-case procedure was applied also to six finely polished samples, to find the fatigue limit in ideal surface conditions, $\Delta\sigma_{f0}$. With the series OXXOOX (Fig. 5) a Dixon's coefficient of -0.831, leading, according to Equation (2), to a fatigue limit of 697 MPa. Analogously to as-built specimens, literature values of fatigue limits for SLM Ti6Al4V polished specimens (tested at R = 0.1), vary significantly, due to differences in the type of powder, printing process parameters and surface conditions that were adopted. However, again, the obtained value falls well within the range found in literature, which varies between 600 MPa and 800 MPa [75–77]. Indeed, Syed et al. [75], found a fatigue limit of 600 MPa for SLM specimens with$R_a = 0.2$ μm, Wycisk et al. [76] obtained 680 ± 35 MPa for manually polished specimens, while Heimbrook and Gall [77] measured a fatigue limit of 800 MPa for$R_a = 0.070$ μm. The higher performance is probably ascribable to the fact that the specimens underwent a hot isostatic press treatment. The fatigue limits of all series of specimens are reported in Table 5.

Thanks to the identification of the ideal fatigue limit of polished specimens, it was possible to calculate the surface finish modification factor (C_f), to account for the influence of surface finish on materials fatigue strength [78]. C_f is defined as the ratio between the fatigue limit obtained with a given surface finish and the theoretical fatigue limit, obtained under ideal surface finish conditions, i.e., the fatigue limit obtained with the third series of specimen (Table 5 and Fig. 6). Such factors represent a practical tool for engineers designing components made from SLM Ti6Al4V. In addition to stair-case tests, in the case of as-built and machined samples tests were also conducted in the finite life region. The resulting stress-life (S-N) diagrams according to Wöhler [49] are shown in Figs. 7 and 8, respectively.

Table 3
Quasi-static material parameters.

Material	σ_Y[MPa]	UTS [MPa]	K[MPa]	n[-]	E[GPa]
as-built	957	1071	1310	0.05	102
machined	1028	1162	1410	0.05	105

Table 4
Surface roughness of the as-built and the machined specimens – average of three measurement per specimen.

Roughness [μm]	As-built	Machined	Polished
R_a	48.6	0.69	0.12
R_t	279.0	7.12	1.12
R_z	254.9	5.90	0.79
R_v	111.1	3.86	0.51

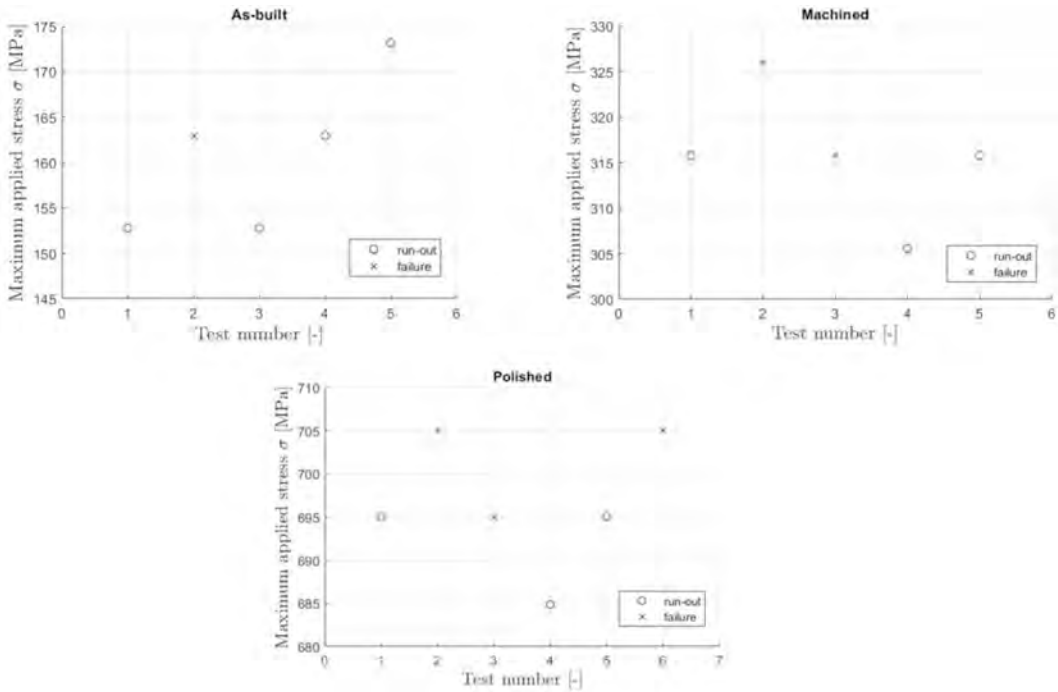

Fig. 5. Stair-case testing sequence of as-built, machined and polished samples.

Table 5
Fatigue limits and reduction factors due to surface finish.

Material	as-built	machined	polished
$\Delta\sigma_f$[MPa]	161	319	694
C_f[-]	0.23	0.46	1

3.3. LCF tests

The cyclic Ramberg-Osgood parameters that were obtained are reported in Table 6, while the corresponding curves can be observed in Fig. 9 and Fig. 10. Both the stabilized curves (as-built and machined) show softening behavior, which is typical of Ti6Al4V [79–81]. With regard to the Basquin-Coffin-Manson curves, they are displayed in Fig. 11, while the corresponding parameters (obtained with the tuning procedure discussed in Section 2.3) are listed in Table 6.

3.4. Metallographic analysis

Metallographic observations revealed almost no porosity in the specimens. Besides, in all analyzed specimens no contour layer was observed. After chemical etching, in both the transversal and the longitudinal planes only slight evidence of the melt pools were visible (Fig. 12). At higher magnifications, a needle-like microstructure was observed, compatible with the α' martensite. SEM observations confirmed this morphology.

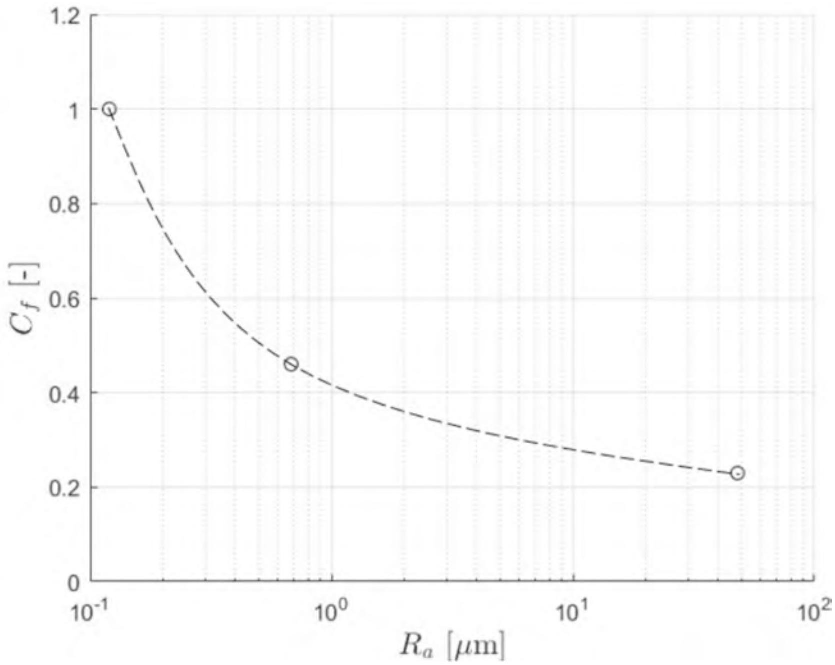

Fig. 6. Fatigue limit reduction factors due to surface roughness.

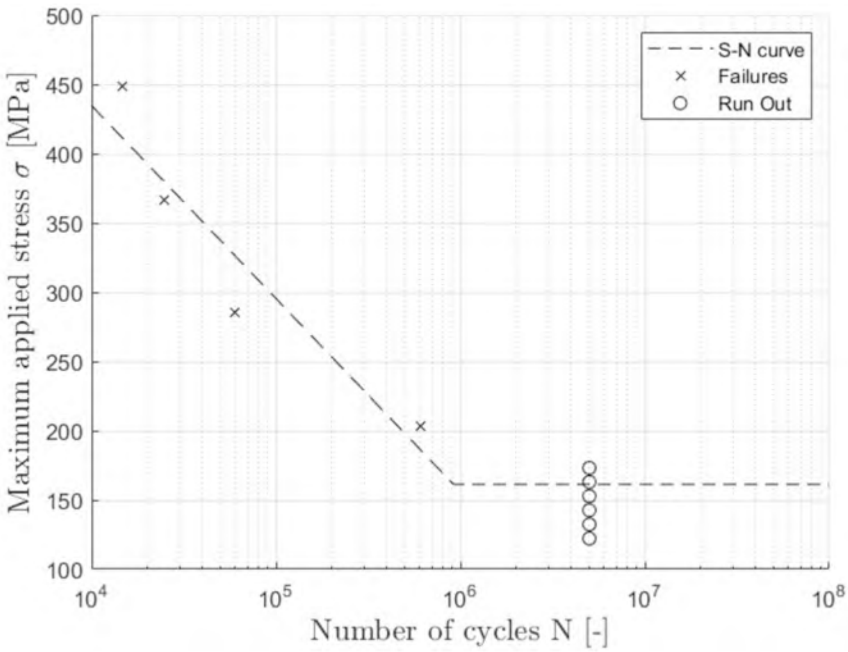

Fig. 7. S-N curve of as-built specimens.

3.5. *Fracture surface investigation*

The observation of HCF and especially LCF fracture surfaces was quite complicated, as high loads reduced the propagation zones. Moreover, some defects were observed on the fracture surfaces of both HCF and LCF specimens, probably occurred when the final fracture happened. Nevertheless, an extensive SEM investigation was performed to identify the nucleation, propagation and fracture zones. In observed LCF and HCF specimens, the crack nucleation, sometime single and sometime multiple, originated from surface roughness and defects. In the machined specimens, fatigue failure started from the surface as well, because of the residual roughness

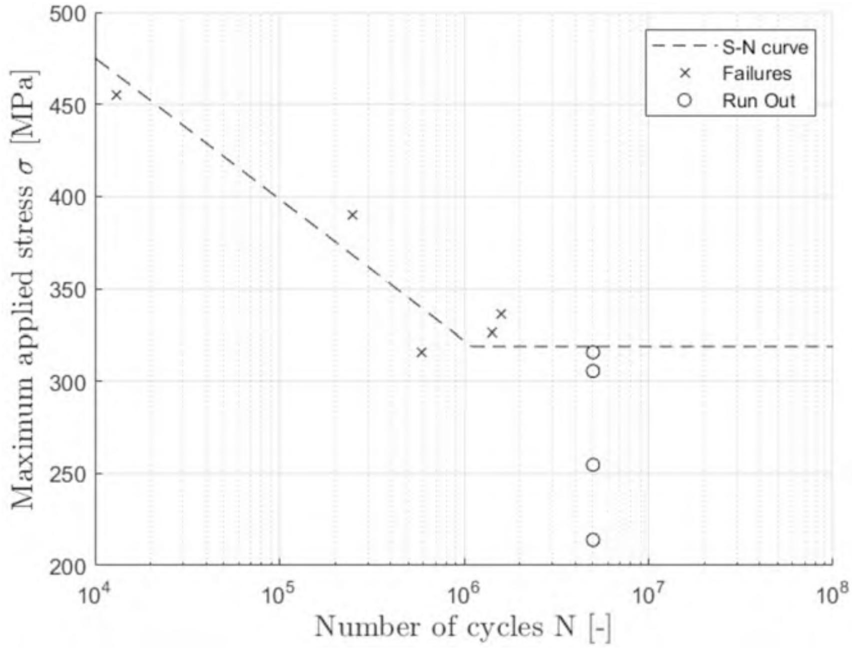

Fig. 8. S-N curve of machined specimens.

Table 6
Cyclic Ramberg-Osgood and Basquin-Coffin-Manson parameters.

Material	K'_{RO} [MPa]	n'_{RO} [-]	σ'_f [MPa]	ε'_f [−]	b[−]	c[−]
as-built	1310	0.058	985	0.0130	−0.128	−0.290
machined	1505	0.084	1090	0.0221	−0.095	−0.136

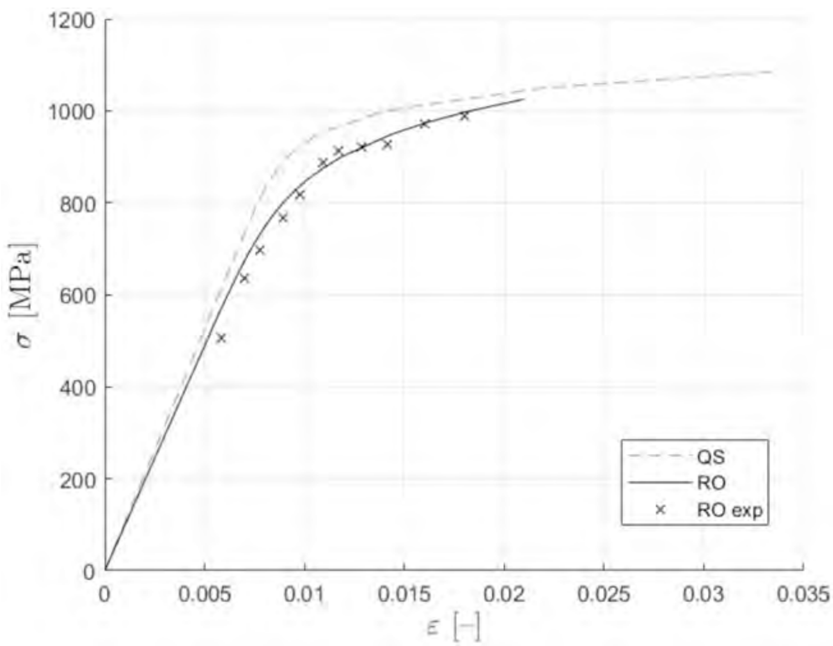

Fig. 9. Ramberg-Osgood cyclic curve (RO), quasi static curve (QS), and experimental stabilized loads (RO exp), for as-built samples.

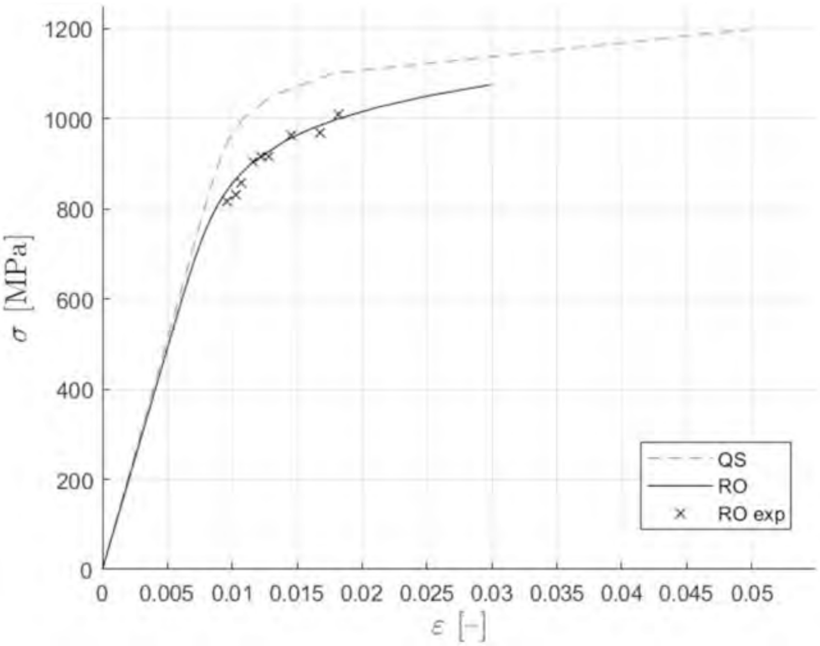

Fig. 10. Ramberg-Osgood cyclic curve (RO), quasi static curve (QS), and experimental stabilized loads (RO exp), for machined samples.

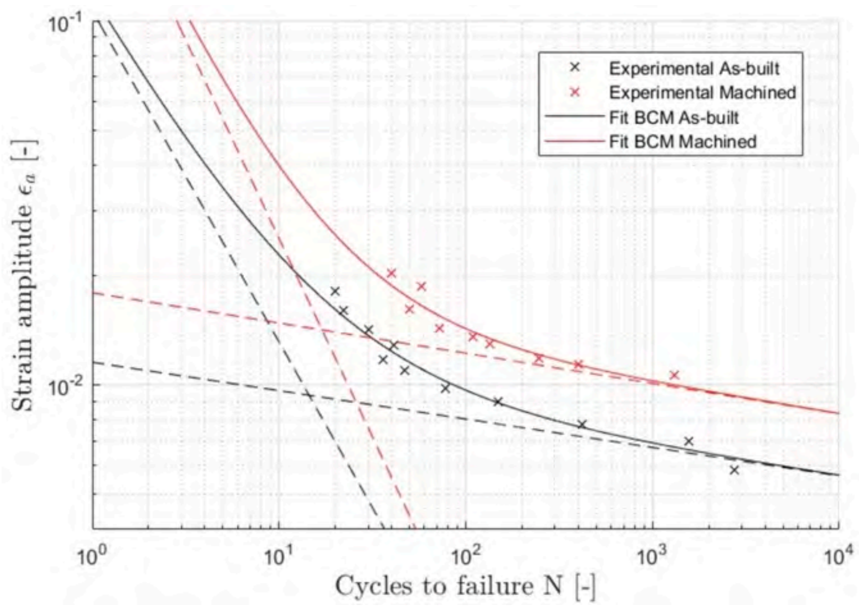

Fig. 11. BCM diagram of both machined and as-built samples.

related to machining process. For all the analyzed samples, the final fracture is characterized by very small dimples associated with a micro-ductile mechanism. The observed samples are summarized in Table 7.

Regarding the surface presented in Fig. 13 (specimen HCF-AB), the final fracture morphology suggests that the nucleation zone is located on the opposite side of the specimen as highlighted by the green and yellow lines. Moreover, the ratchet mark reveals the presence of two propagation areas. The larger one refers to the crack that nucleated first. Observing the nucleation zone in the upper-right side of Fig. 13a, a large defect (Defect 1) was identified. This is the probable origin of the fatigue failure, thus it was used as nucleation-triggering defect for the fracture mechanics analysis of specimen HCF-AB (Section 3.6). The observation of the other nucleation zone revealed the presence of a smaller, but sharp defect (Defect 2) highlighted in Fig. 13c. In the fatigue failure shown in Fig. 14 (specimen HCF-AB2), the morphology of the final fracture is similar to the one reported in Fig. 13. The main nucleation zone is

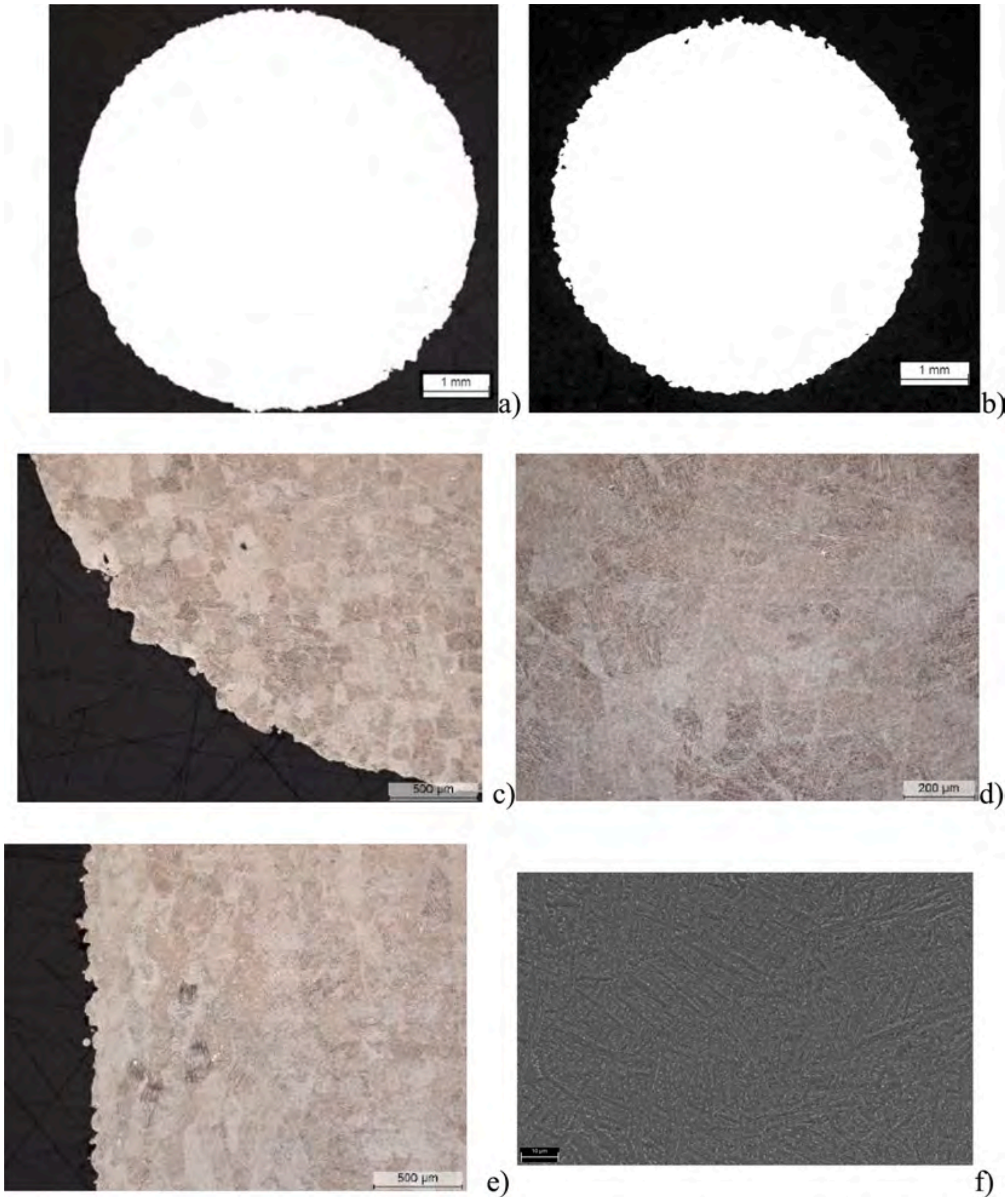

Fig. 12. As-built condition. Mirror-polished transversal section showing almost no residual porosity (a, b). Microstructure observed in transversal (c, d) and longitudinal directions (e). SEM image in the transversal plane (f).

Table 7
Samples used for SEM analysis of fracture surfaces and fatigue micro-mechanisms.

Type	Series	ID	Number of cycles to failure
As-built	High-cycle fatigue	HCF-AB	24,652
As-built	High-cycle fatigue	HCF-AB2	605,715
As-built	Low-cycle fatigue	LCF-AB	36
Machined	High-cycle fatigue	HCF-M	588,499
Machined	Low-cycle fatigue	LCF-M	109

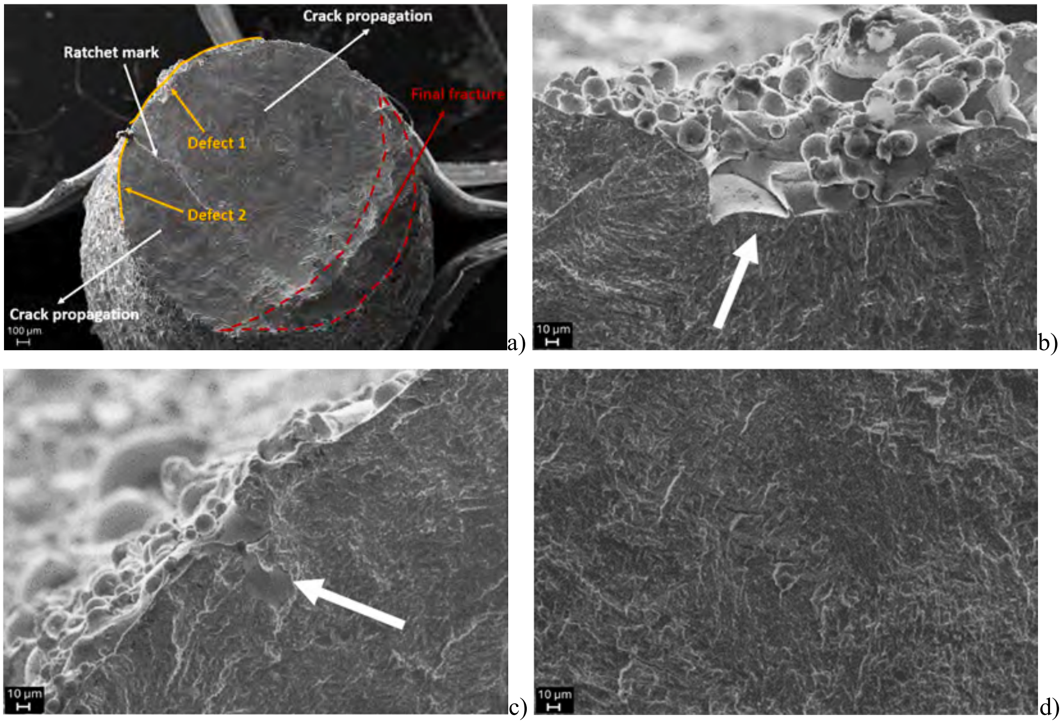

Fig. 13. Fracture surface analysis of specimen HCF-AB – (a) fracture surface, (b) nucleation zone of Defect 1, (c) nucleation zone of Defect 2, (d) propagation zone.

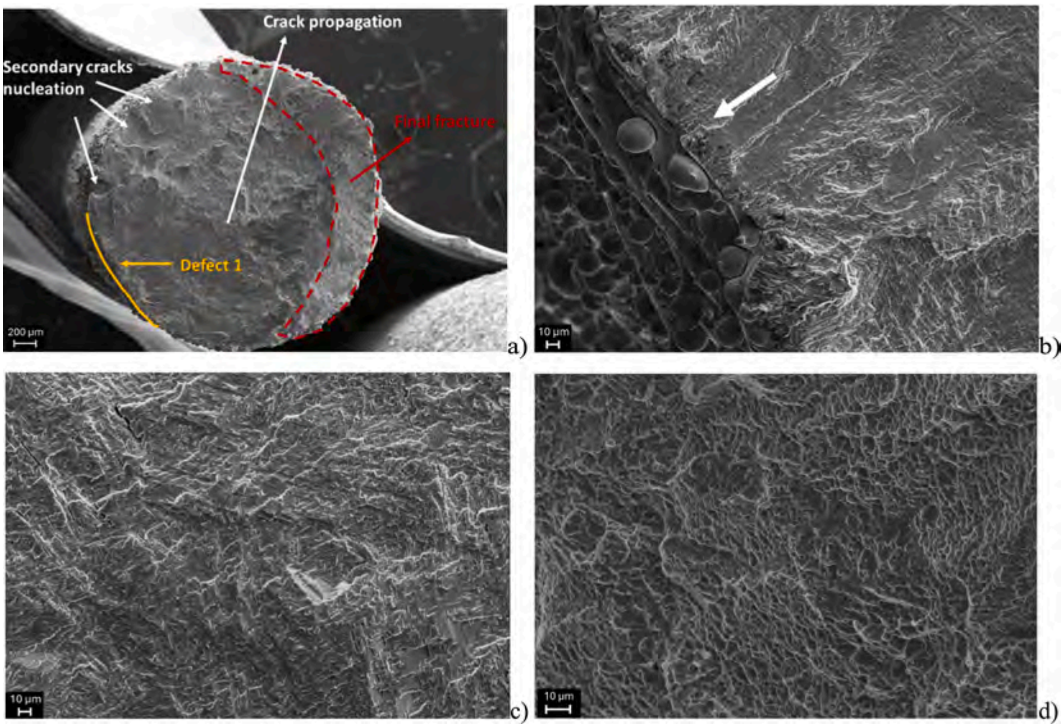

Fig. 14. Fracture surface analysis of specimen HCF-AB2 – (a) fracture surface, (b) magnification of Defect 1 – some radial marks are visible too, (c) propagation zone, (d) fracture zone.

located on the opposite side of the specimen (marked by a yellow line). A careful observation in that area revealed the presence of a sharp defect, probably a lack of fusion, that is compatible with the origin of the fatigue failure. Hence, this defect was used as nucleation-triggering defect for the fracture mechanics analysis of specimen HCF-AB (Section 3.6). In the upper-left side of Fig. 14a, secondary cracks nucleation can be seen.

Regarding HCF machined samples, the fracture surfaces were very complicated and often damaged. One example is shown in Fig. 15 (specimen HCF-M). In order to identify possible surface defects related to the building process, the whole perimeter of the fracture surface was observed. No defects were detected. This is compatible with the very low residual porosity characterizing the investigated material. After the removal of the outer surface, in fact, the only defects that can appear on the machined surface are inner pores located close to the as-built original skin. This suggests that the fatigue failure was probably originated from the surface roughness due to the machining operation. Thus, for specimen HCF-M, in the fracture mechanics analysis performed in Section 3.6, roughness was chosen as failure-triggering defect.

With regard to the LCF fracture surfaces, one as-built specimen is shown in Fig. 16 (specimen LCF-AB) and one machined specimen is showed in Fig. 17 (specimen LCF-M). The final fractures in the two specimens are highlighted in Fig. 16a and 17a, respectively. Their shape suggests that crack nucleation occurred on the opposite surfaces as remarked by the yellow lines. In case of specimen LCF-AB it was very complicated to identify the very first onset of the fatigue failure, but a deep investigation of the nucleation zone revealed the presence of three sharp defects highlighted in Fig. 16a, 16b and 16c. For specimen LCF-M, the fracture surface perimeter was observed as described by Fig. 17, finding no clear defect different from the surface roughness.

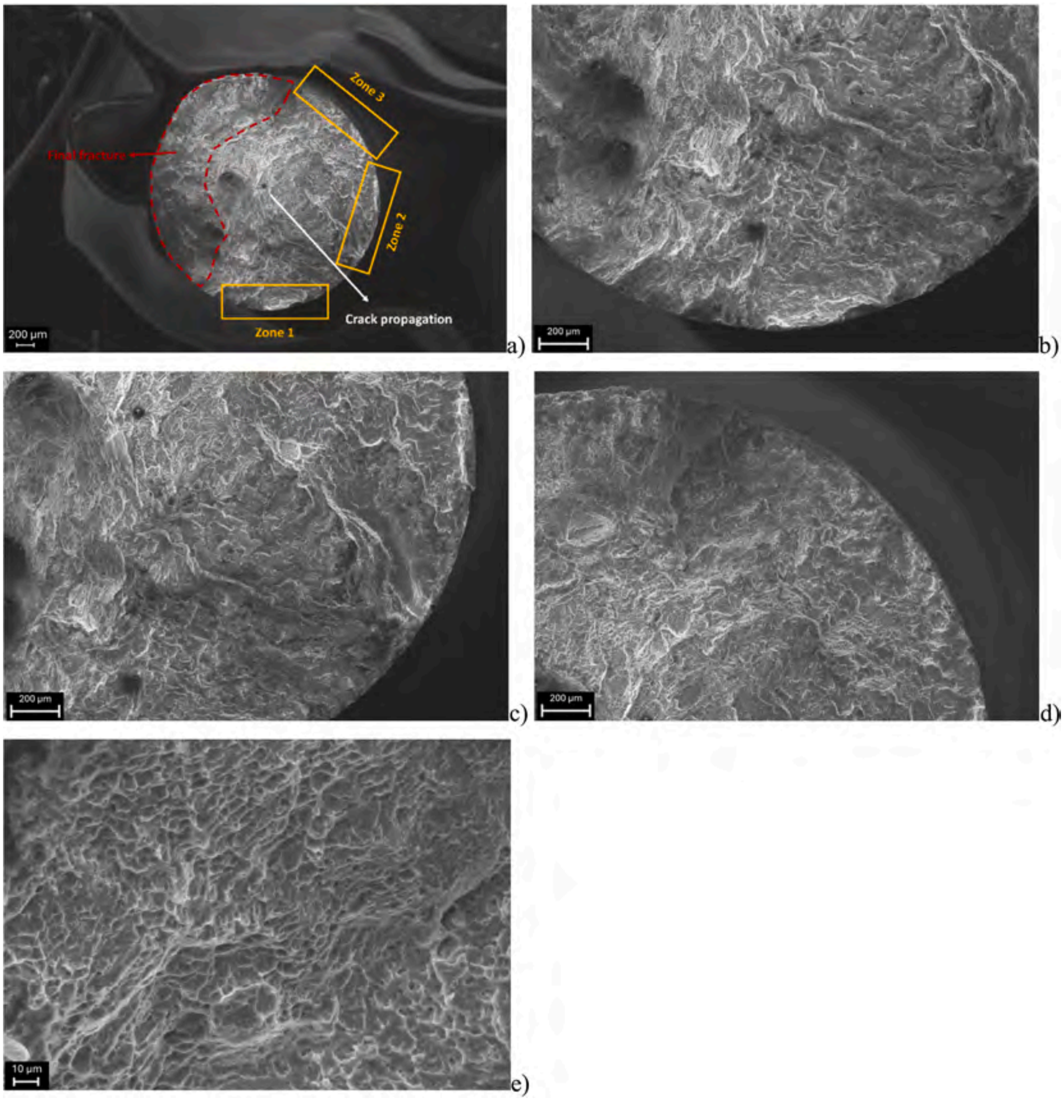

Fig. 15. Fracture surface analysis of specimen HCF-M – (a) fracture surface, (b) magnification of Zone 1, (c) magnification of Zone 2, (d) magnification of Zone 3, (e) fracture zone.

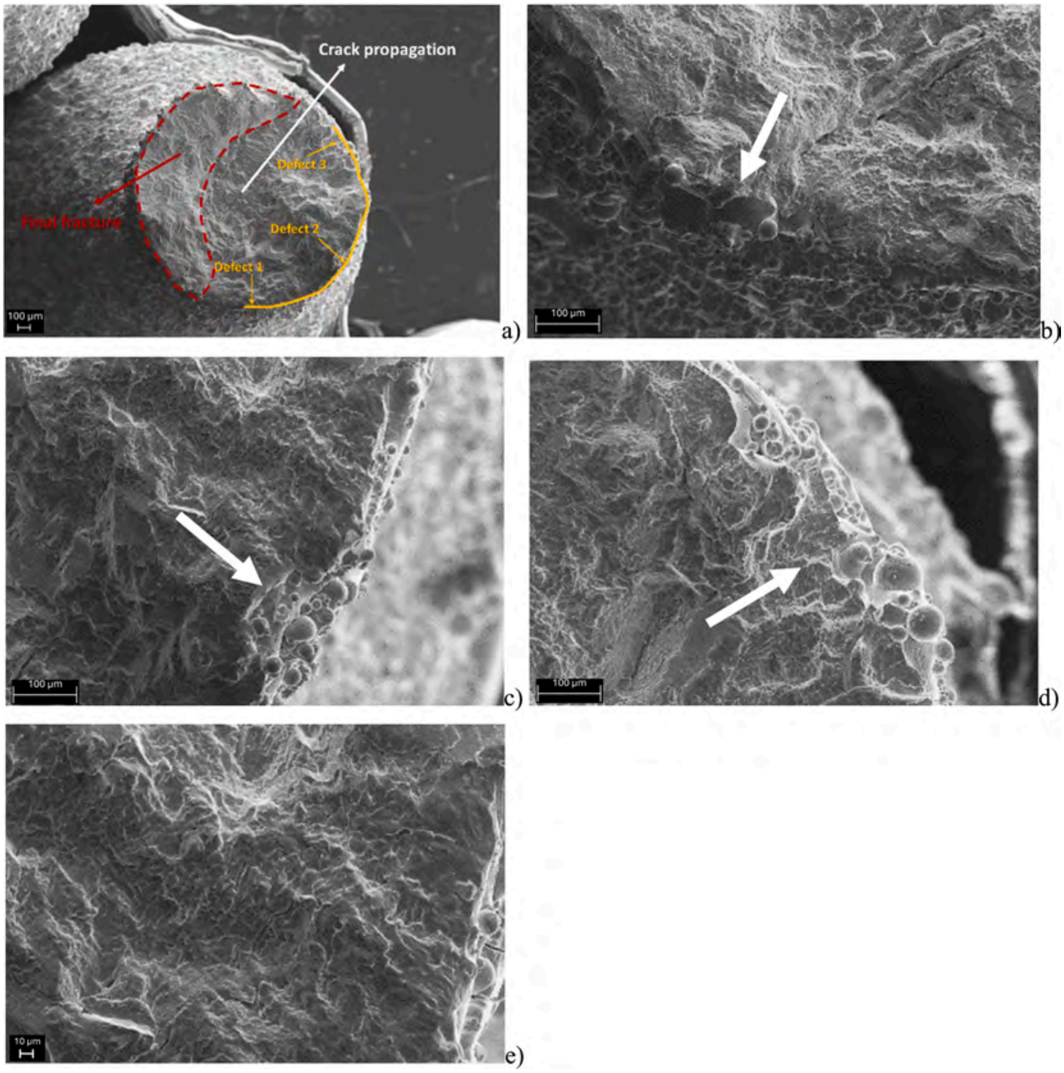

Fig. 16. Fracture surface analysis of specimen LCF-AB – (a) fracture surface, (b) nucleation zone n.1, (c) nucleation zone n.2 (d) nucleation zone n.3, (e) propagation zone.

3.6. Fracture mechanics analysis and Kitagawa-Takahashi diagrams

For all the specimens analysed with Murakami's approach [55] (HCF-AB, HCF-AB2 and HCF-M) surface roughness, surface defects and inner defects were converted into equivalent micro-notches. With regard to specimens HCF-AB and HCF-AB2, the crack nucleation occurred because of the combined influence of roughness notch effect and near-surface defects (as identified in Section 3.5). In the case of specimen HCF-AB2, the nucleation defect has a length-to-width ratio higher than 10, making it a shallow defect (Equation (13). As far as specimen HCF-M is concerned, the crack nucleated due to the roughness notch effect only. Treating the surface roughness as a shallow defect, it was converted into an equivalent micro-notch length as $\sqrt{10}R_v$. Surface and inner defects were converted using the $\sqrt{area}$ parameter, measured form the defect area as shown in Fig. 18 for sample HCF-AB and HCF-AB2. The equivalent micro-notch parameters for all three samples are displayed in Table 8. The limit curves describing non-propagating cracks regions were computed according to Equation (14), Equation (18) and Equation (20) (Fig. 19a for specimen HCF-AB, Fig. 20a for specimen HCF-AB2, Fig. 21a for specimen HCF-M). Using Equation (20), the limit curves of samples HCF-AB and HCF-AB2 were computed (Fig. 19b and Fig. 20b, respectively) considering the notch, the roughness and the combination of notch and roughness effects. In specimen HCF-M, the fracture was caused only due to the roughness, so only the roughness effect was considered. In all cases the ideal fatigue limit ($\Delta\sigma_{f0}$) was set as the fatigue limit obtained using the finely-polished specimens.

The non-propagating regions were hence defined for every specimen with three different laws, and for all possible combination of defect-roughness notch effects (except for specimen HCF-M, where only roughness caused failure). For both specimen HCF-AB and specimen HCF-AB2, Equation (18) and Equation (20) produced very similar curves, almost overlapping. In the case of specimen HCF-

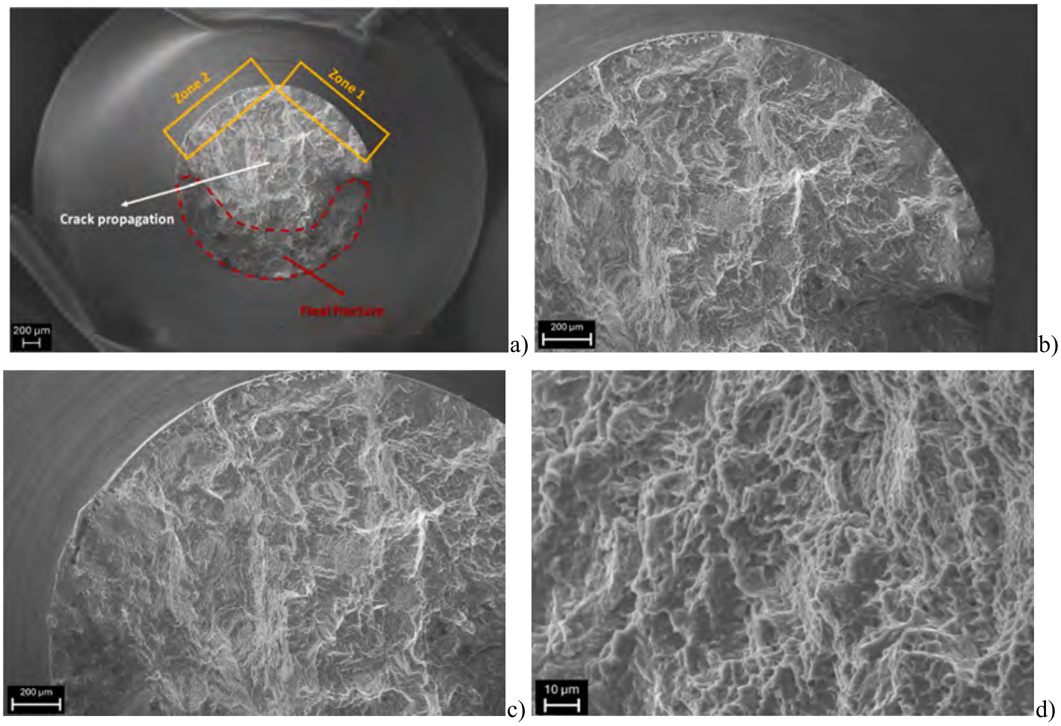

Fig. 17. Fracture surface analysis of specimen LCF-M – (a) fracture surface, (b) magnification of Zone 1, (c) magnification of Zone 2, (d) final fracture.

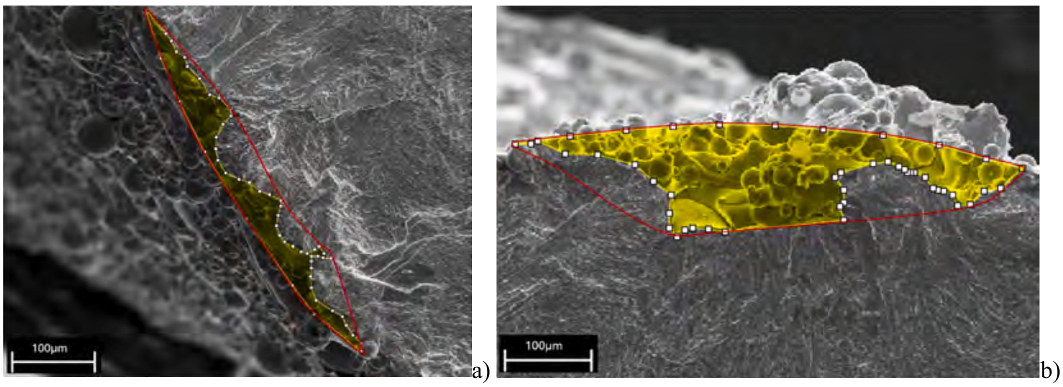

Fig. 18. Determination of nominal area (yellow area) and convex effective area (red line) for defect HCF-AB2 (a) and HCF-AB (b), as showed in Fig. 2. (For interpretation of the references to colour in this figure legend, the reader is referred to the web version of this article.)

AB2 (Fig. 20) the failure lies well outside all non-propagating regions, while for specimen HCF-AB (Fig. 19) the failure lies near the El-Haddad's curve (Equation (14), which is the least conservative curve. Its lower conservativity is confirmed with specimen HCF-M, whose failure lies exactly at the border between propagating and non-propagating regions according to EL-Haddad's curve (Fig. 21). It should be added that the value of R_v which was used to calculate the equivalent defect area, was very similar for all the machined specimens, and therefore an average value was considered and associated to all machined samples. For this reason, the K-T diagram for specimen HCF-M can be used to plot also the failures of other HCF specimens (observable in Fig. 8), in the case they were also caused by the micro-notch effect of roughness. Such failures and are compared in a detail-view of HCF-M K-T diagram (Fig. 21b). Even when higher loads are involved, the failure lies outside the non-propagating regions defined by Equation (18) and Equation (20), but within the region defined by El-Haddad's law (Equation (14).

4. Conclusions

In this experimental testing campaign, cylindrical specimens produced via SLM were tested to determine the fatigue behavior of AM

Table 8
Micro-notch data of analysed specimens.

ID	Nucleation site	Surface roughness R_v [μm]	Micro-notch (roughness) [μm]	$\sqrt{area}$(defect) [μm]	Micro-notch total length [μm]	Failure stress [MPa]
HCF-AB	Defect	111.1	351.3	213.3	564.6	203.7
HCF-AB2	Defect	111.1	351.3	205.5	556.8	366.7
HCF-M	Surface roughness	3.86	12.2	–	12.2	315.8

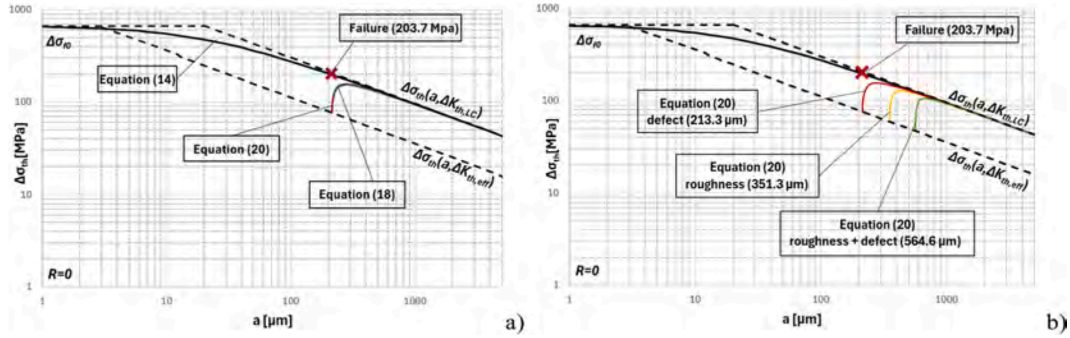

Fig. 19. Specimen HCF-AB. Comparison of the limit curves for non-propagating cracks in the K-T diagram (a) and comparison of the curve described by Equation (20) for different equivalent micro-notch lengths (b).

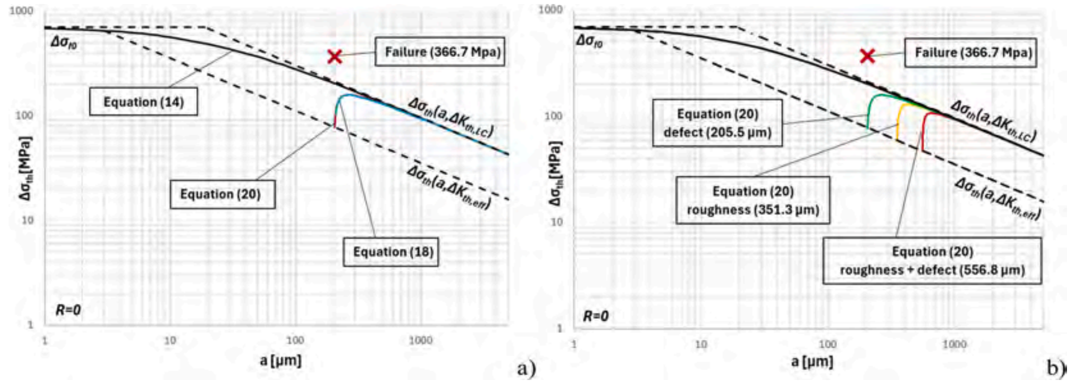

Fig. 20. Specimen HCF-AB2. Comparison of the limit curves for non-propagating cracks in the K-T diagram (a) and comparison of the curve described by Equation (20) for different equivalent micro-notch lengths (b).

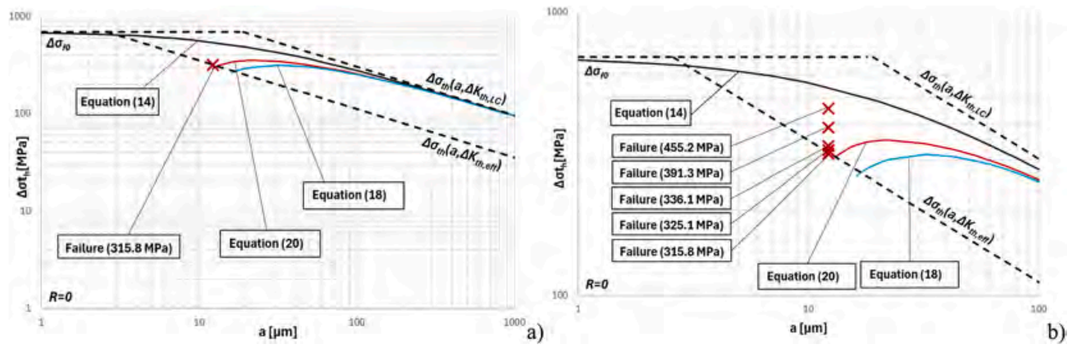

Fig. 21. Specimen HCF-M. Comparison of the limit curves for non-propagating cracks in the K-T diagram (a) and comparison of HCF failures of other machined samples (b).

Ti6Al4V and the influence of surface roughness. Three series of samples, each having different surface finish conditions (as-built, machined and polished) were employed. No samples underwent heat treatment, and their dimensions were chosen to be representative of the characteristic strut size of AM reticular structures. The as-built and machined series were characterized in terms of roughness, monotonic, LCF and HCF behaviors. The polished series was intended to determine the fatigue limit under ideal surface finish conditions only, undergoing roughness and HCF tests only. The fatigue limit was estimated using the short staircase approach. From the LCF results, the Ramberg-Osgood equation was tuned and the BCM parameters calibrated to fit the actual data. Both series show a marked softening behavior. The HCF limits significantly differ between the as-built ($\Delta\sigma_f = 161$ MPa), the machined condition ($\Delta\sigma_f = 319$ MPa) and the polished series ($\Delta\sigma_f = 694$ MPa), quantifying the effect of surface roughness, which promotes the nucleation of cracks that lead to a premature failure. This allowed the determination of the fatigue limit reduction factors due to surface finish, providing designers with a practical tool for evaluating the effect of surface roughness on the fatigue performance of additively manufactured Ti6Al4V. Selected specimens belonging to the as-built and the machined series were observed by SEM after the LCF and HCF tests. In all cases, surface single or multiple nucleation was detected: for the as-built condition, this is related to the very bad surface condition, whereas in the machined ones, it is related to the residual roughness left by the machining operation. Fractures were analyzed according to Murakami's theory, and Kitagawa-Takahashi diagrams were plotted for the selected specimens, obtaining the limit curves for non-propagating cracks considering the total equivalent micro-notch of both the surface roughness and surface/inner defects. El-Haddad's approach demonstrated to be the least conservative approach, as already observed in the literature. When the limit curve associated to the total equivalent micro-notch of both the surface roughness and killer defect is considered, the specimen failure was always justified.

CRediT authorship contribution statement

L. Pagliari: Writing – review & editing, Writing – original draft, Visualization, Validation, Methodology, Investigation, Formal analysis, Data curation, Conceptualization. **R. Gerosa:** Writing – original draft, Validation, Supervision, Methodology, Investigation, Formal analysis, Data curation, Conceptualization. **D. Panzeri:** Investigation, Data curation. **L. Fraccaroli:** Investigation, Data curation. **F. Concli:** Validation, Supervision, Methodology, Conceptualization.

Declaration of competing interest

The authors declare that they have no known competing financial interests or personal relationships that could have appeared to influence the work reported in this paper.

Data availability

Data will be made available on request.

References

[1] T.D. Ngo, A. Kashani, G. Imbalzano, K.T.Q. Nguyen, D. Hui, Additive Manufacturing (3D printing): a review of materials, methods, applications and challenges, Compos. B Eng. 143 (2018) 172–196, https://doi.org/10.1016/j.compositesb.2018.02.012.
[2] R. O'Leary, R. Setchi, P. Prickett, G. Hankins, N. Jones, An investigation into the recycling of ti-6al-4v powder used within slm to improve sustain- ability, SDM'2015 2nd Int, Conf. Sustain. Des. Manuf. 2 (2015) 14–17.
[3] F. Concli, A. Gilioli, F. Nalli, Experimental–numerical assessment of ductile failure of Additive Manufacturing selective laser melting reticular structures made of Al A357, Proc. Inst. Mech. Eng. C J. Mech. Eng. Sci. 235 (10) (2019), https://doi.org/10.1177/0954406219832333.
[4] F. Concli, Z. Alomar, A Review of the Selective Laser Melting Lattice Structures and their Numerical Models, Adv. Eng. Mater. 22 (12) (2020), https://doi.org/10.1002/adem.202000611.
[5] C. Buchanan, L. Gardner, Metal 3D printing in construction: a review of methods, research, applications, opportunities and challenges, Eng. Struct. 180 (2019) 332–348, https://doi.org/10.1016/j.engstruct.2018.11.045.
[6] L. Pagliari, L. Fraccaroli, F. Concli, Numerical Analysis of the Impact of Shot Peening on the Tooth Root Strength of AlSi10Mg Gears Using Critical Plane Multiaxial Fatigue Criteria. In: Borgianni, Y., Matt, D.T., Molinaro, M., Orzes, G. (eds) Towards a Smart, Resilient and Sustainable Industry. ISIEA 2023. Lecture Notes in Networks and Systems, vol 745. Springer, Cham. doi:10.1007/978-3-031-38274-1_56.
[7] L.J. Tan, W. Zhu, K. Zhou, Recent Progress on Polymer Materials for Additive Manufacturing, Advanced Functional Materials 30 (2020), https://doi.org/10.1002/adfm.202003062.
[8] M. Rafiee, R.D. Farahani, D. Therriault, Multi-Material 3D and 4D printing: a Survey, Adv. Sci. 7 (12) (2020), https://doi.org/10.1002/advs.201902307.
[9] Y. Lakhdar, C. Tuck, J. Binner, A. Terry, R. Goodridge, Additive manufacturing of advanced ceramic materials, Progress in Material Science 116 (2021). doi: 101016./j.pmatsci.2020.100736.
[10] G. Liu, X. Zhang, X. Chen, Y. He, L. Cheng, M. Huo, J. Yin, F. Hao, S. Chen, P. Wang, S. Yi, L. Wan, Z. Mao, Z. Chen, X. Wang, Z. Cao, J. Lu, Additive manufacturing of structural materials, Mater. Sci. Eng. R. Rep. 145 (2021), https://doi.org/10.1016/j.mser.2020.100596.
[11] I.M. Kusoglu, B. Gökce, S. Barcikowski, Research trends in laser powder bed fusion of Al alloys within the last decade, Addit. Manuf. 36 (2) (2020), https://doi.org/10.1016/j.addma.2020.101489.
[12] D. Zhang, S. Sun, D. Qiu, M.A. Gibson, M.S. Dargusch, M. Brandt, M. Qian, M. Easton, Metal Alloys for Fusion-based Additive Manufacturing, Adv. Eng. Mater. 20 (5) (2018), https://doi.org/10.1002/adem.201700952.
[13] R. Gandhi, L. Maccioni, F. Concli, Significant Advancements in Numerical simulation of Fatigue Behavior in Metal Additive Manufacturing-Review, Appl. Sci. 12 (21) (2022), https://doi.org/10.3390/app122111132.
[14] J.H. Martin, B.D. Yahata, J.M. Hundley, J.A. Mayer, T.A. Schaedler, T.M. Pollock, 3D printing of high-strength aluminium alloys, Nature 549 (7672) (2017) 365–369, https://doi.org/10.1038/nature23894.
[15] W.J. Sames, F.A. List, S. Pannala, R.R. Dehoff, S.S. Babu, The metallurgy and processing science of metal additive manufacturing, Int. Mater. Rev. 61 (5) (2016) 315–360, https://doi.org/10.1080/09506608.2015.1116649.
[16] C. Cui, B. Hu, L. Zhao, S. Liu, Titanium alloy production technology, market prospects and industry development, Mater. Des. 32 (3) (2011) 1684–1691, https://doi.org/10.1016/j.matdes.2010.09.011.
[17] R. Boyer, An overview on the use of titanium in the aerospace industry, Mater. Sci. Eng. A 213 (1–2) (1996) 103–114, https://doi.org/10.1016/0921-5093(96)10233-1.
[18] D. Kotzem, D. Tazerout, T. Arold, T. Niendorf, F. Walther, Failure mode map for E-PBF manufactured Ti6Al4V sandwich panels, Eng. Fail. Anal. 121 (2021) 105159, https://doi.org/10.1016/j.engfailanal.2020.105159.
[19] E. Uhlmann, R. Kersting, T. Klein, M. Cruz, A. Borille, Additive Manufac- Turing of Titanium Alloy for Aircraft Components 35 (2015) 55–60, https://doi.org/10.1016/j.procir.2015.08.061.
[20] A. Sedmak, F. Vucetic, K. Colic, A. Grbovic, S. Sedmak, S. Kirin, F. Berto, Fatigue life assessment of orthopedic plates made of Ti6Al4V, Eng. Fail. Anal. 137 (2022) 106259, https://doi.org/10.1016/j.engfailanal.2022.106259.
[21] Q. Shi, Y. Sun, S. Yang, J. Van Dessel, H.T. Lübbers, S. Zhong, Y. Gu, M. Bila, T. Dormaar, J. Schoenaers, C. Politis, Failure analysis of an in-vivo fractured patient-specific Ti6Al4V mandible reconstruction plate fabricated by selective laser melting, Eng. Fail. Anal. 124 (2021) 105353, https://doi.org/10.1016/j.engfailanal.2021.105353.

[22] R. Gandhi, M. Salmi, B. Roy, L. Pauli, L. Pagliari, F. Concli, Mechanical and fatigue performance of multidirectional functionally graded Ti6Al4V scaffolds produced via laser powder bed fusion for orthopedic implants, Mater. Des. (2025) 113725.
[23] J. Giannatsis, V. Dedoussis, Additive fabrication technologies applied to medicine and health care: a review, Int. J. Adv. Manuf. Technol. 40 (1–2) (2009) 116–127, https://doi.org/10.1007/s00170-007-1308-1.
[24] L. Ciocca, M. Fantini, F. De Crescenzio, G. Corinaldesi, R. Scotti, Direct metal laser sintering (dmls) of a customized titanium mesh for prostheti- cally guided bone regeneration of atrophic maxillary arches, Med. Biol. Eng. Comput. 49 (11) (2011) 1347–1352, https://doi.org/10.1007/s11517-011-0813-4.
[25] R. Huang, M. Riddle, D. Graziano, J. Warren, S. Das, S. Nimbalkar, J. Cresko, E. Masanet, Energy and emissions saving potential of addi- tive manufacturing: the case of lightweight aircraft components, Jour- nal of Cleaner, Production 135 (2016) 1559–1570, https://doi.org/10.1016/j.jclepro.2015.04.109.
[26] D. Herzog, V. Seyda, E. Wycisk, C. Emmelmann, Additive manufacturing of metals, Acta Materialia 117 (2016) 371–392. doi:10. 1016/j.actamat.2016.07.019.
[27] W. Frazier, Metal additive manufacturing: a review, J. Mater. Eng. Perform. 23 (6) (2014) 1917–1928, https://doi.org/10.1007/s11665-014-0958-z.
[28] M. Avateffazeli, M. Haghshenas, Ultrasonic fatigue of laser beam powder bed fused metals: a state-of-the-art review, Eng. Fail. Anal. 134 (2022) 106015, https://doi.org/10.1016/j.engfailanal.2021.106015.
[29] Y. Shin, N. Bailey, C. Katinas, W. Tan, Predictive modeling capabilities from incident powder and laser to mechanical properties for laser directed energy deposition, Comput. Mech. 61 (5) (2018) 617–636, https://doi.org/10.1007/s00466-018-1545-1.
[30] C. Katinas, S. Liu, Y. Shin, Self-sufficient modeling of single track deposi- tion of ti-6al-4v with the prediction of capture efficiency, Journal of Man- Ufacturing Science and Engineering, Transactions of the ASME 141 (1) (2019), https://doi.org/10.1115/1.4041423.
[31] S. Liu, Y. Shin, Simulation and experimental studies on microstructure evolution of resolidified dendritic TiCx in laser direct deposited Ti-TiC composite, Mater. Des. 159 (2018) 212–223, https://doi.org/10.1016/j.matdes.2018.08.053.
[32] L. Parry, I. Ashcroft, R. Wildman, Understanding the effect of laser scan strategy on residual stress in selective laser melting through thermo- mechanical simulation, Addit. Manuf. 12 (2016) 1–15, https://doi.org/10.1016/j.addma.2016.05.014.
[33] S.N. Singh, A.B. Deoghare, High layer thickness laser directed energy deposition of Ti6Al4V alloy: Microstructure, fatigue behavior and fractography, Eng. Fail. Anal. 148 (2023) 107208, https://doi.org/10.1016/j.engfailanal.2023.107208.
[34] M. Strantza, R. Vafadari, D. De Baere, B. Vrancken, W. Van Paepegem, I. Vandendael, H. Terryn, P. Guillaume, D., Van Hemelrijck, Fatigue of ti6al4v structural health monitoring systems produced by selective laser melting, Materials 9 (2) (2016), https://doi.org/10.3390/ma9020106.
[35] T. Risposi, L. Rusnati, L. Patriarca, A. Hardaker, D. Luczyniec, S. Beretta, Fatigue of Ti6Al4V manufactured by PBF-LB: a comparison of failure mechanisms between net-shape and electro-chemically milled surface conditions, Eng. Fail. Anal. 172 (2025) 109403, https://doi.org/10.1016/j.engfailanal.2023.107208.
[36] Y.N. Hu, S.C. Wu, P.J. Withers, J. Zhang, H.Y.X. Bao, Y.N. Fu, G.Z. Kang, The effect of manufacturing defects on the fatigue life of selective laser melted Ti-6Al-4V structures, Mater. Des. 192 (2020), https://doi.org/10.1016/j.matdes.2020.108708.
[37] T.H. Becker, P. Kumar, U. Ramamurty, Fracture and fatigue in additively manufactured metals, Acta Mater. 219 (2021), https://doi.org/10.1016/j.actamat.2021.117240.
[38] ASTM, Standard practice for conducting force controlled constant amplitude axial fatigue tests of metallic materials, International standard; ASTM E466 ASTM E466.
[39] ASTM, Strain controlled fatigue testing, International standard; ASTM E606 ASTM E606.
[40] F. Concli, L. Fraccaroli, F. Nalli, L. Cortese, High and low-cycle-fatigue properties of 17–4 ph manufactured via selective laser melting in as-built, machined and hipped conditions, Prog. Addit. Manuf. 7 (1) (2022) 99–109, https://doi.org/10.1007/s40964-021-00217-y.
[41] F. Concli, R. Gerosa, D. Panzeri, L. Fraccaroli, High-and low-cycle-fatigue properties of additively manufactured Inconel 625, Prog. Addit. Manuf. 9 (6) (2024) 1921–1940, https://doi.org/10.1007/s40964-023-00545-1.
[42] L. Maccioni, L. Fraccaroli, Y. Borgianni, F. Concli, High-cycle-fatigue characterization of an additive manufacturing 17-4 ph stainless steel, Key Engineering Materials 877 KEM (2021) 49–54. doi:10.4028/www.scientific. net/KEM.877.49.
[43] W. Ramberg, W. R. Osgood, Description of stress–strain curves by three parameters, Technical Note No. 902 (1943) National Advisory Committee For Aeronautics, Washington DC, USA.
[44] W. Dixon, The up-and-down method for small samples, Journal of the American Statistical Association 60 (312) (1965) 967–978. doi:10.1080/ .
[45] F. Concli, Austempered ductile iron (ADI) for gears: contact and bending fatigue behavior, Procedia Struct. Integrity 8 (2018) 14–23, https://doi.org/10.1016/j.prostr.2017.12.003.
[46] C. Gorla, F. Rosa, E. Conrado, F. Concli, Bending fatigue strength of case carburized and nitrided gear steels for aeronautical applications, Int. J. Appl. Eng. Res. 12 (21) (2017) 11306–11322.
[47] C. Gorla, E. Conrado, F. Rosa, F. Concli, Contact and bending fatigue behaviour of austempered ductile iron gears, Proc. Inst. Mech. Eng. C J. Mech. Eng. Sci. 232 (6) (2018) 998–1008, https://doi.org/10.1177/0954406217695846.
[48] F. Concli, R. Gerosa, D. Panzeri, L. Fraccaroli, High and low cycle fatigue properties of selective laser melted AISI 316L and AlSi10Mg, Int. J. Fatigue 177 (2023), https://doi.org/10.1016/j.ijfatigue.2023.107931.
[49] A. Wöhler, Theorie rechteckiger eiserner brückenbalken mit gitterwänden und mit blechwänden, Zeitschrift Für Bauwesen 5 (1855) 121–166.
[50] L. Maccioni, E. Rampazzo, F. Nalli, Y. Borgianni, F. Concli,877 KEM, Low-cycle- fatigue properties of a 17-4 ph stainless steel manufactured via selective laser melting, Key Eng. Mater. (2021) 55–60, https://doi.org/10.4028/www.scientific.net/KEM.877.55.
[51] O. Basquin, The exponential law of endurance tests, in: Proc Am Soc Test Mater, Vol. 10, 1910, pp. 625–630.
[52] S. S. Manson, Behavior of Materials Under Condition of Thermal Stress, Technical Note No. 2933 (1953) National Aeronautics and Space Administration Washington, DC, USA.
[53] L.F. Coffin, A Study of the Effects of Cyclic thermal Stresses on a Ductile Metal, ASME Transactions 76 (6) (1954) 931–949, https://doi.org/10.1115/1.4015020.
[54] ASTM, Standard test method for permeation of liquids and gases through protective clothing materials under conditions of continuous contact, Inter- national standard; ASTM 739 ASTM 739.
[55] Y. Murakami, Metal Fatigue: Effects of Small Defects and Nonmetallic Inclusions, Elsevier (2002), https://doi.org/10.1016/B978-0-08-044064-4.X5000-2.
[56] S. Beretta, M. Gargourimotlagh, S. Foletti, A. du Plessis, M. Riccio, Fatigue strength assessment of "as built" AlSi10Mg manufactured by SLM with different build orientations, Int. J. Fatigue 139 (2020) 105737, https://doi.org/10.1016/j.ijfatigue.2020.105737.
[57] H. Kitagawa, Applicability of fracture mechanics to very small cracks or the cracks in the early stage, in: In: Proceedings 2nd International Conference on Mechanical Behaviour of Materials, 1976, pp. 627–631.
[58] M.H. El Haddad, K.N. Smith, T.H. Topper, Fatigue crack propagation of short cracks, J. Eng. Mater. Technol. 101 (1979) 42–46, https://doi.org/10.1115/1.3443647.
[59] K. Tanaka, Y. Akiniwa, Resistance-curve method for predicting propagation threshold of short fatigue cracks at notches, Eng. Fract. Mech. 30 (1988) 863–876, https://doi.org/10.1016/0013-7944(88)90146-4.
[60] R. Pippan, M. Berger, H.P. Stüwe, The influence of crack length on fatigue crack growth in deep sharp notches, Metall. Mater. Trans. A 18 (3) (1987) 429–435.
[61] M. Chapetti, Fatigue propagation threshold of short cracks under constant amplitude loading, Int. J. Fatigue 25 (2003) 1319–1326, https://doi.org/10.1016/S0142-1123(03)00065-3.
[62] A.J. McEvily, K. Minakawa, On crack closure and the notch size effect in fatigue, Eng. Fract. Mech. 28 (1987) 519–527, https://doi.org/10.1016/0013-7944(87)90049-X.
[63] U. Zerbst, M. Madia, Fracture mechanics based assessment of the fatigue strength: approach for the determination of the initial crack size, Fatigue Fract. Eng. Mater. Struct. 38 (2015) 1066–1075, https://doi.org/10.1111/ffe.12288.
[64] B. Li, L.G. Rosa, Prediction models of intrinsic fatigue threshold in metal alloys examined by experimental data, Int. J. Fatigue 82 (2016) 616–623, https://doi.org/10.1016/j.ijfatigue.2015.09.018.
[65] R. Pippan, F. O. Riemelmoser, Modeling of fatigue crack growth: Dislocation models, in: Comprehensive structural integrity, Elsevier (2003) 191–207. doi: 10.1016/B0-08-043749-4/04035-0.

[66] D. Hull, D. J. Bacon, Introduction to dislocations, (2011) Elsevier.
[67] J. Maierhofer, H.P. Gänser, R. Pippan, Modified Kitagawa-Takahashi diagram accounting for finite notch depths, Int. J. Fatigue 70 (2015) 503–509, https://doi.org/10.1016/j.ijfatigue.2014.07.007.
[68] J. Cho, Characterization of the α'-Martensite phase and its decomposition in Ti-6Al-4V additively manufactured by selective laser melting, RMIT University, 2018. Doctoral dissertation.
[69] E. Wycisk, A. Solbach, S. Siddique, D. Herzog, F. Walther, C. Emmelmann, Effects of Defects in Laser Additive Manufactured Ti-6Al-4V on Fatigue Properties, Phys. Procedia 56 (2014) 371–378, https://doi.org/10.1016/j.phpro.2014.08.120.
[70] W. Xu, S. Sun, J. Elambasseril, Q. Liu, M. Brandt, M. Qian, Ti-6Al-4V Additively Manufactured by Selective Laser Melting with Superior Mechanical Properties, JOM 67 (2015) 668–673, https://doi.org/10.1007/s11837-015-1297-8.
[71] S., Bagehorn, T., Mertens, D., Greitemeier, L., Carton, A. Schoberth, Surface finishing of additive manufactured Ti-6Al-4V-a comparison of electrochemical and mechanical treatments. In *6th Eur conf aerosp sci.* (2015).
[72] E. Wycisk, C. Emmelmann, S. Siddique, F. Walther, High Cycle Fatigue (HCF) performance of Ti-6Al-4V Alloy Processed by Selective Laser Melting, Adv. Mat. Res. 816–817 (2013) 134–139, https://doi.org/10.4028/www.scientific.net/amr.816-817.134.
[73] H. Gong, K. Rafi, H. Gu, G.D. Janaki Ram, T. Starr, B. Stucker, Influence of defects on mechanical properties of Ti-6Al-4V components produced by selective laser melting and electron beam melting, Mater. Des. 86 (2015) 545–554, https://doi.org/10.1016/j.matdes.2015.07.147.
[74] D. Greitemeier, F. Palm, F. Syassen, T. Melz, Fatigue performance of additive manufactured TiAl6V4 using electron and laser beam melting, Int. J. Fatigue 94 (2017) 211–217, https://doi.org/10.1016/j.ijfatigue.2016.05.001.
[75] A.K. Syed, W. Vesga, B. Dutton, T. Berentshaw, X. Zhang, Defect tolerance and fatigue limit prediction for laser powder bed fusion Ti6Al4V, Int. J. Fatigue 184 (2024) 108285, https://doi.org/10.1016/j.ijfatigue.2021.106268.
[76] E. Wycisk, S. Siddique, D. Herzog, F. Walther, C. Emmelmann, Fatigue performance of laser additive manufactured Ti–6Al–4V in very high cycle fatigue regime up to 10^9 cycles, Front. Mater. 2 (2015) 72, https://doi.org/10.3389/fmats.2015.00072.
[77] A. Heimbrook, K. Gall, Effect of surface topography on the fatigue behavior of additively manufactured Ti6Al4V and CoCr alloys, Mater. Sci. Eng. A 909 (2024) 146821, https://doi.org/10.1016/j.msea.2024.146821.
[78] F. Curà, R. Sesana, Surface factor assessment in HCF for steels by means of empirical and non destructive techniques, Procedia Struct. Integrity 5 (2017) 500–507, https://doi.org/10.1016/j.prostr.2017.07.151.
[79] S. Springer, M. Leitner, T. Gruber, B. Oberwinkler, M. Lasnik, F. Grün, Low-Cycle Fatigue Behavior of Wire and Arc Additively Manufactured Ti-6Al-4V Material, Materials 16 (18) (2023) 6083, https://doi.org/10.3390/ma16186083.
[80] F. Han, B. Tang, H. Kou, J. Li, Y. Deng, Y. Feng, Cyclic softening behavior of Ti–6Al–4V alloy at macro and micro-scale, Mater. Lett. 185 (2016) 115–118, https://doi.org/10.1016/j.matlet.2016.08.119.
[81] A.D. Pertuz-Comas, O.A. González-Estrada, E. Martínez-Díaz, D.F. Villegas-Bermúdez, J.G. Díaz-Rodríguez, Strain-based Fatigue Experimental Study on Ti–6Al–4V Alloy Manufactured by Electron Beam Melting, Journal of Manufacturing and Materials Processing 7 (1) (2023) 25, https://doi.org/10.3390/jmmp7010025.